Nanoscale

RSC Publishing

PAPER

View Article Online
View Journal | View Issue

Cite this: *Nanoscale*, 2013, **5**, 11193

Highly uniform and optical visualization of SERS substrate for pesticide analysis based on Au nanoparticles grafted on dendritic α-Fe_2O_3†

Xianghu Tang,[ab] Wenya Cai,[ac] Liangbao Yang*[a] and Jinhuai Liu*[a]

Received 17th July 2013
Accepted 30th August 2013

DOI: 10.1039/c3nr03671e

www.rsc.org/nanoscale

Here, Au nanoparticles (NPs) grafted on dendritic α-Fe_2O_3 (NPGDF) are designed as a highly uniform surface-enhanced Raman scattering (SERS) substrate with a feature of optical visualization by an optical microscope (OM) system and used for *in situ* detection of pesticide residues that are annually used in agriculture. With this strategy, the dendritic α-Fe_2O_3 has been synthesized by a hydrothermal method and significantly functionalized by an inductively coupled plasma (ICP) apparatus and then Au NPs were grafted on it densely and uniformly. In addition, the profile of NPGDF can be clearly observed using an OM platform of a Raman spectrometer, and the profile of SERS spectral mapping with NPGDF as substrate almost exactly coincides with the OM image, the electron microscope (EM) image and the elemental mapping of NPGDF, which indicates remarkable uniformity of the NPGDF as SERS substrate, thus ensuring the laser beam focuses on the efficient sites of the substrate under the OM platform. Moreover, NPGDF can be dispersed in the liquor and the NPGDF microparticles can be adsorbed on the target surface. Therefore, it can be used for *in situ* detection of pesticide residues on tea leaves, fruits *etc.*, with high sensitivity and reproducibility.

Introduction

As we know, surface-enhanced Raman scattering (SERS) is a powerful technique for detection and characterization that yields rich structural information with ultra-high sensitivity.[1–5] The fact that particle plasmons allow direct coupling of light to resonant electron plasmon oscillations, which are described as surface plasmons, has spurred tremendous research activities in the design and fabrication of high activity SERS substrates.[6–8] SERS effects are typically observed on metallic nanostructures, which are composed of a noble metal (Au, Ag and Cu) for the most part, such as metal layers with nanoscale roughness, and nanoparticles with morphological features and their aggregates.[2–4] Although these traditional substrates lead to a high SERS signal at some local sites, it is not easy to obtain a stable, reproducible and uniform SERS response spanning a wide dynamic range.

An ideal SERS substrate should induce a high signal enhancement, generate a reproducible and uniform response, and should be easily synthesizable.[9] However, to form a highly uniform SERS substrate with high enhancement ability to solve the poor reproducibility of SERS-active sites for real applications remains a challenge in this field due to lack of fabrication strategies that provide adequate control of the resulting assembly/complex structure for SERS substrate over large areas, which is at least several times larger than the spot size of a laser beam, while, it can offer a highly sensitive, uniform and reproducible SERS response. Generally, a complex SERS substrate can either be fabricated by top-down nanolithography techniques or by bottom-up self-assembly.[10] Top-down approaches allow for the production of customized metallic nanostructures with a controllable size, shape, spacing and positioning, but it is difficult to control sub-10 nm gap sizes, a size-domain that is particularly attractive for the generation of plasmonic hot-spots.[11,12] On the other hand, bottom-up approaches adopt self-assembly processing techniques to construct complex nanostructures with small gap sizes, but it is difficult to achieve highly uniform structures across a large area.[13–16] Furthermore, it is well known that most of the Raman signal acquisition is carried out on an optical microscope (OM) platform, while the nanostructure of the SERS substrate is characterized by electron microscopy (EM). That is, the nanostructure of the SERS substrate cannot be observed on the OM platform when a Raman signal is collected. Thus, it cannot ensure the laser beam focuses on the efficient sites of the substrate. Therefore, from the application viewpoint, it is necessary to develop a strategy with an efficient SERS substrate that can not only provide strong enhancement factors, but can also display both the large area of uniform and localized

[a]*Institute of Intelligent Machines, Chinese Academy of Sciences, Hefei 230031, China. E-mail: lbyang@iim.ac.cn; jhliu@iim.ac.cn; Fax: +86 551-65592420*

[b]*School of Chemistry and Materials Science, University of Science and Technology of China, Hefei 230026, P.R. China*

[c]*School of Chemistry and Chemical Engineering, Anhui University, Hefei, 230039, China*

† Electronic supplementary information (ESI) available: Fig. S1–S11. See DOI: 10.1039/c3nr03671e

nanoscale structures, while being stable and reproducible. No matter what area of the substrate is illuminated by the laser beam focus, the SERS response should be as uniform as possible and should be easily observed while Raman signal acquisition is carried out on the OM platform.

Herein, with emphasis on methodology, we rationally designed Au nanoparticles (NPs) grafted on dendritic α-Fe_2O_3 (NPGDF) as a highly uniform SERS substrate with a feature of optical visualization by OM system and used it for *in situ* detection of pesticide residues that are annually used in agriculture. Scheme 1 illustrates the difference between random NPs film substrate and optical visualization substrate. Scheme 1A reveals that some sites of the random NPs film substrate are not uniform. At the same time, the NPs or aggregates cannot be observed by OM, but can be seen only under EM (indicated by the magnifier), which causes it to not being able to ensure the laser beam focus on the efficient sites. Scheme 1B shows the optical visualization substrate. By means of a series of processes, Au NPs were densely grafted on a two-dimensional (2-D) dendritic α-Fe_2O_3 surface. Here, it is worth noting that the reason for picking 2-D dendritic α-Fe_2O_3 is to avoid the impact of the surface fluctuation on the focusing problem of the laser beam. The NPGDF in the scale of several micrometres and its profile can be visualized clearly under the OM system. Therefore, this substrate is with a well-defined boundary and Au NPs assembled uniformly, which can ensure the laser beam focuses on the efficient sites of the substrate within the boundary. In general, by the OM platform of Raman spectrometer, we will make the texture of the substrate as clear as seen through the OM image corresponding to the nanostructure of the substrate observed by EM. Besides, NPGDF can be dispersed in the liquor and the NPGDF microparticles can be adsorbed on the target surface. Thus, it can be used for *in situ* detection of pesticide residues on tea leaves, fruits *etc*. with high sensitivity and reproducibility. And in addition, it was durable and stable under air ambient conditions for months. The details are shown below.

Experimental

Materials

Trisodium citrate, $K_3Fe(CN)_6$, $HAuCl_4 \cdot 4H_2O$ and ethanol were purchased from Shanghai Chemical Reagent Co. Ltd. 3-Aminopropyltrimethoxysilane (APTMS), 4-aminothiophenol (4-ATP), crystal violet (CV) and thiram were purchased from Sigma-Aldrich. All reagents are of analytical grade and used without further purification.

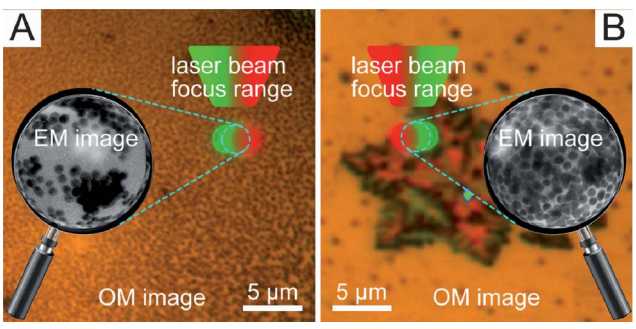

Scheme 1 Schematic illustration of the difference between (A) random NPs film substrate and (B) optical visualization substrate. The EM image is indicated within the magnifier.

Synthesis of dendritic α-Fe_2O_3 and modification by plasma treatment (PT)

The synthesis was carried out according to the literature[17] with a small modification. A typical experiment to synthesize dendritic α-Fe_2O_3 was as follows: first, 0.1317 g $K_3Fe(CN)_6$ powder was dispersed in 40 mL water to form a 10 mM homogeneous solution under stirring, then the solution was sealed in a 50 mL autoclave, and maintained at 220 °C for 24 h. After that, the autoclave was cooled gradually to room temperature. The red precipitates were collected by centrifugation, and washed with deionized water and ethanol three times, and finally dried in vacuum at 60 °C for 6 h. And then the as-synthesized dendritic α-Fe_2O_3 was treated by an inductively coupled plasma (ICP) apparatus.[18] The radio frequency (RF) power at a frequency of 13.5 MHz was fed to the copper wire. The experimental procedure was as follows: 0.5 g dendritic α-Fe_2O_3 was put into the flask and evacuated to about 10 Pa. The system was flushed with argon gas, and then evacuated back to 10 Pa again. After three cycles of flushing and evacuation, the dendritic α-Fe_2O_3 powders were treated with argon/oxygen (ratio of flow 5 : 1) plasma for 30 min under stirring. Finally, the plasma-treated dendritic α-Fe_2O_3 was dried in vacuum at 60 °C for 6 h and stored at room temperature.

Synthesis of Au nanoparticles (NPs)

Au NPs were synthesized by reduction of $HAuCl_4$ using trisodium citrate.[19,20] Typically, freshly prepared aqueous trisodium citrate solution (2 mL, 1 wt%) was quickly added to a boiling aqueous solution of $HAuCl_4$ (100 mL, 0.25 mM) under vigorous stirring and refluxing. After several minutes, the color of the solution changed from blue to brilliant red. After boiling for 40 min, the heat source was removed to allow the reaction solution to cool to room temperature, and it was subsequently stored at 4 °C in fridge.

Grafting dendritic α-Fe_2O_3 with Au NPs

First, 1 mL APTMS was dissolved in 100 mL ethanol and stirred at room temperature for 10 min, followed by 0.1 g as-pretreated dendritic α-Fe_2O_3 powders being added under vigorous stirring for 24 h. Then, the suspended particles were collected by centrifugation and washed with ethanol three times, followed by drying in vacuum at 60 °C for 6 h. Next, as-synthesized Au NPs solution was added to the above treated dendritic α-Fe_2O_3. The reaction was allowed to proceed at room temperature for 1 h under continuous mechanical stirring with ultrasonication. This process was repeated twice and the resulting products were collected by centrifugation followed by washing with water. After that, the products were redispersed in 10 mL water with ultrasonication prior to further use. The preparation process can be seen in Fig. S1, ESI.†

Characterization

The morphology, structure and composition of the samples were investigated by using a Quanta 200FEG field emission scanning electronic microscope (FESEM), a Philips X-Pert Pro X-ray diffractometer (XRD) with Cu Ka radiation ($\lambda K\alpha 1$ = 1.5418 Å), a JEOL JEM-2010 High-resolution transmission electron microscope (HRTEM) equipped with an Oxford INCA energy dispersive spectroscopy (EDS) system at an accelerating voltage of 200 kV, respectively. The elemental mappings and the area scans were carried out in the high-angle annular dark-field (HAADF) mode on the same HRTEM. X-Ray photoelectron spectroscopy (XPS) analysis used non-monochromatized Mg Kα X-ray beams as the excitation source in an ESCALab MK II instrument. Raman spectra were carried out on a LabRAM HR800 confocal microscope Raman system (Horiba Jobin Yvon) using a He–Ne laser operating at 632.8 nm. The laser beam was focused on the sample with a size of about 1.5 μm using a 50× LMPLFLN microscope objective. The laser power was approximately 1 mW and the exposure time was 3 s for each spectrum. SERS spectral mapping was collected using 1 s exposure time and the step size was 0.4 μm.

Results and discussion

The formation of dendritic α-Fe_2O_3 crystals and Au NPs was characterized by the XRD pattern and UV–vis absorption spectra, respectively (Fig. S2 and S3, ESI†). The evidence for Au NPs grafted on dendritic α-Fe_2O_3 was confirmed by the XPS spectra, as shown in Fig. 1. Fig. 1A illustrates the XPS spectra of (a) pure dendritic α-Fe_2O_3, (b) dendritic α-Fe_2O_3 with PT, (c) PT dendritic α-Fe_2O_3 with APTMS, and (d) Au NPs grafted on dendritic α-Fe_2O_3. Besides, Fig. 1B shows the corresponding high-resolution spectra of O1s region of (a) and (b), which are indicated by the olive circle in (A). Seen from the spectra of O1s in Fig. 1B, the peak around 531.2 eV can be ascribed to the Fe–OH group. By comparing the ratio of Fe–OH to Fe–O peak areas of the XPS spectra before and after plasma treatment, it can be found that the density of –OH groups has been increased greatly by plasma treatment. It is indicated that the dendritic α-Fe_2O_3 has been significantly functionalized by using PT, which facilitates its achieving dense modification of APTMS and grafting Au NPs. As compared with (a), (b) and (c), the peak of N1s (indicated by the pink circle in Fig. 1A) appeared after further modification with APTMS, which can be ascribed to the amino group. And after Au NPs were grafted on dendritic α-Fe_2O_3, the peak of Au could be easily found.

In addition, the morphology of the obtained NPGDF was characterized by SEM (Fig. 2) and TEM (Fig. 3A and B correspond to different magnifications). Fig. 2A and B show pure dendritic α-Fe_2O_3 without any modification. The product almost entirely consists of 2-D dendritic structures, indicating the high yield and uniformity of the dendrites. The length of the dendrite trunk is about ten more micrometers and the secondary branches are about 3–5 μm for the most part. Fig. 2C and D illustrate the dendritic α-Fe_2O_3 with PT, from which the dendritic structures can still be seen clearly. Fig. 2E and F

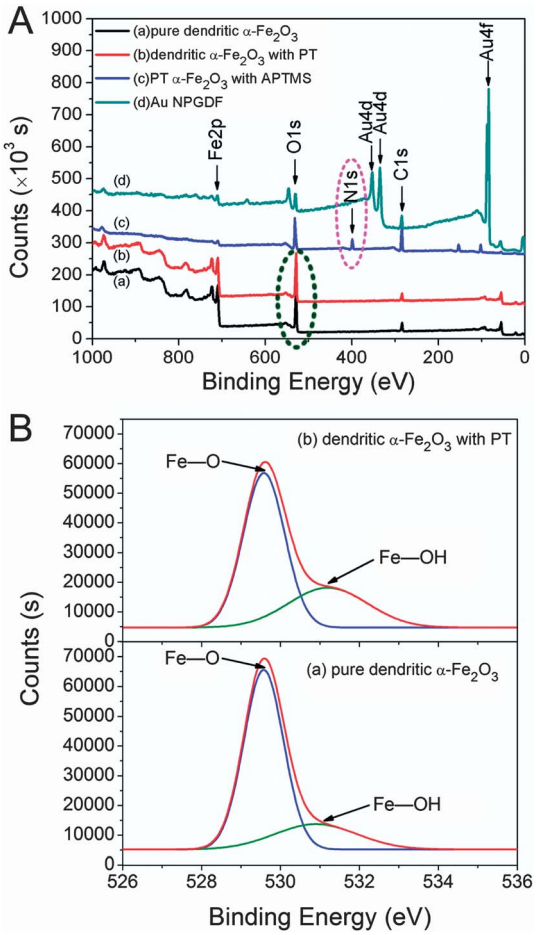

Fig. 1 (A) XPS spectra of (a) pure dendritic α-Fe_2O_3, (b) dendritic α-Fe_2O_3 with PT, (c) PT dendritic α-Fe_2O_3 with APTMS, and (d) Au NPs grafted on dendritic α-Fe_2O_3. (B) The corresponding high-resolution spectra of O1s region of (a) and (b), indicated by the olive circle in (A).

indicate Au NPs grafted on dendritic α-Fe_2O_3 without PT, while Fig. 2G and H show Au NPs grafted on dendritic α-Fe_2O_3 with PT corresponding to different magnifications. Compared with Fig. 2E–H, it is clearly revealed that the Au NPs were grafted on dendritic α-Fe_2O_3 surface with PT more densely. This indicates that the grafted density of Au is greatly enhanced by the PT method. Moreover, as can be clearly seen from Fig. 3A and B, the Au NPs were grafted on the dendritic α-Fe_2O_3 surface densely. In order to further investigate the elemental distribution of the NPGDF, the elemental mappings of O, Fe and Au were also performed by EDS area scans corresponding to Fig. 3A, as shown in Fig. 3C (the EDS spectrum can be seen in Fig. S4, ESI†). From Fig. 3C, the profile of Au La1 is very close to that of O Ka1 and Fe Ka1, which indicates that the Au element distributes uniformly and densely throughout the entire structure. Besides, seen from the gap distance distribution of Au NPs of NPGDF (Fig. 3D, insets illustrate the specific measurements of Au NPs size and gap distance distribution of interparticle separations, more details can be seen in Fig. S5, ESI†), it is also revealed that the Au NPs were grafted on dendritic α-Fe_2O_3 surface uniformly. It is worth mentioning that there were many gaps of several nm with a narrow size distribution between Au

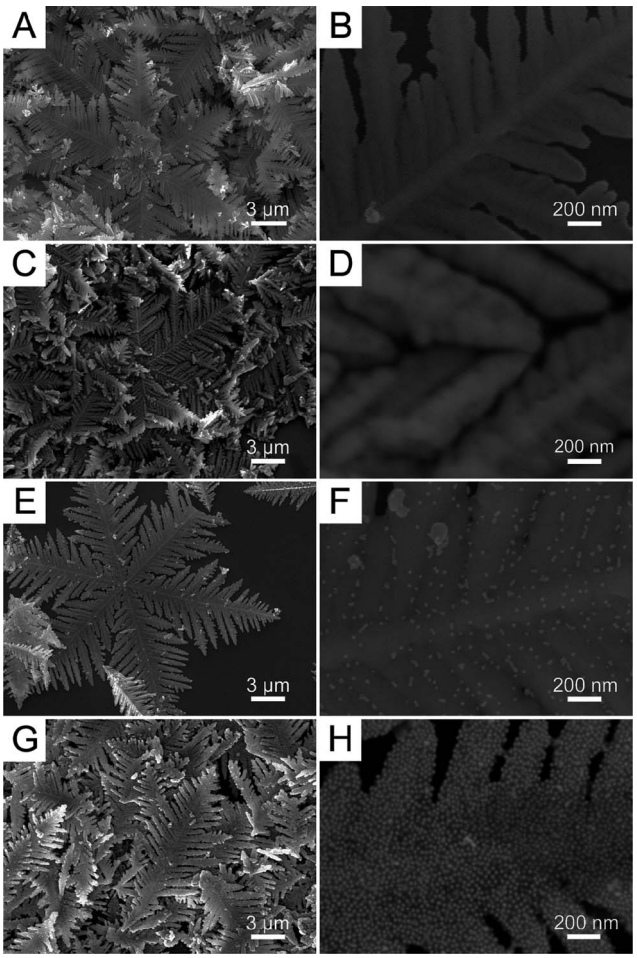

Fig. 2 Typical SEM images of the samples. (A and B) Pure dendritic α-Fe_2O_3 crystals without any modification. (C and D) Dendritic α-Fe_2O_3 crystals with plasma treatment (PT). (E and F) Au NPs grafted on dendritic α-Fe_2O_3 without PT. (G and H) Au NPs grafted on dendritic α-Fe_2O_3 with PT correspond to different magnifications.

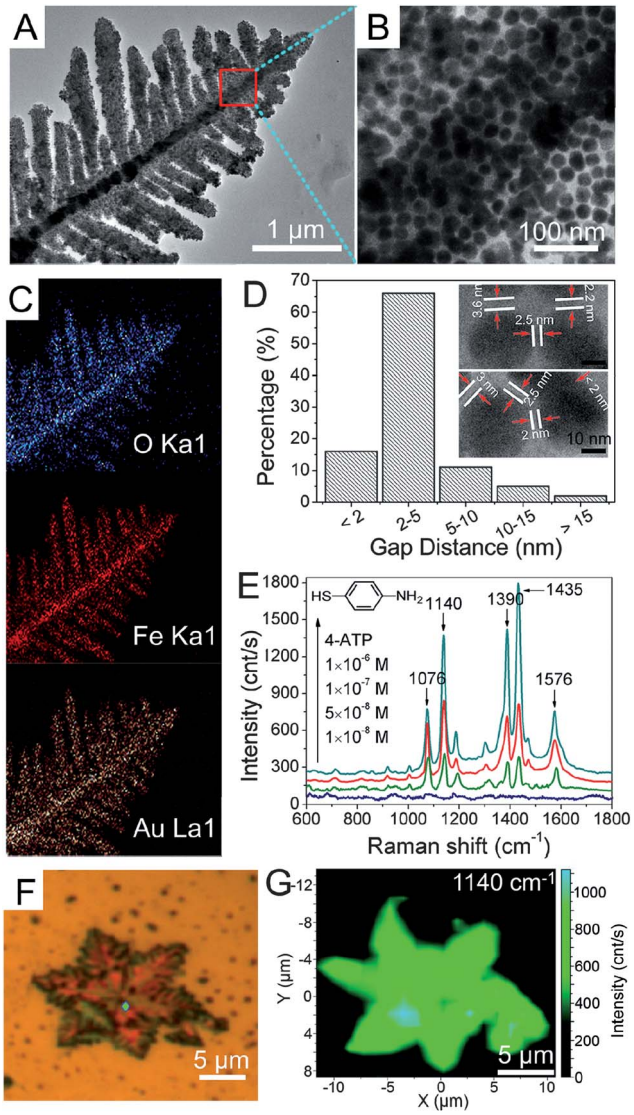

Fig. 3 Characterization of Au NPs grafted on dendritic α-Fe_2O_3. (A) and (B) Typical TEM images correspond to different magnifications. (C) Elemental mappings of O Ka1, Fe Ka1 and Au La1 corresponding to (A). (D) Gap distance distribution of Au NPs and the specific measurements of Au NPs interparticle separations (insets). (E) Series of SERS spectra of 4-ATP at different concentrations. (F) Optical image by OM platform of Raman spectrometer. (G) SERS spectral mapping corresponding to (F) based on the intensity of the spectral band at 1140 cm^{-1} of 10^{-6} M 4-ATP.

NPs, especially 93% of the gap distance less than 10 nm, and most of them distributed around 2–5 nm, which would be very advantageous for forming hot spots and achieving large near-field enhancement effects, and being beneficial for SERS activity.[21,22]

To evaluate the potential application of as-obtained NPGDF as SERS substrate, 4-ATP was chosen as the probe molecule. For preparation of SERS substrates, 20 μL of NPGDF suspension (Fig. S6, ESI†) was carefully dropped on the specially cleaned Si wafers followed by 20 μL adding a given concentration of 4-ATP solution. After the mixture was completely dried under air ambient conditions, the Raman spectra were carried out. Fig. 3E reveals the series of SERS spectra of 4-ATP at different concentrations with NPGDF as the substrates. The results clearly show that the determination capability of our SERS probe was below 5×10^{-8} M, that is, the NPGDF exhibits good SERS activity and sensitivity as SERS substrate. The primary vibrations of 4-ATP are confirmed according to our previous work[23] and the literature.[24–26] Two sets of bands were observed on the SERS spectra of 4-ATP on the surface of Au NPs. One set is located at 1076 and 1576 cm^{-1}, which is assigned to the a1 vibrational modes and the other set is located at 1140, 1390 and 1435 cm^{-1}, which is assigned to the b2 vibrational modes. In order to observe the enhancement intuitively and quantitatively, the SERS enhancement factor (EF)[26–29] was calculated as follows:

$$\mathrm{EF} = \frac{I_{\mathrm{SERS}}/N_{\mathrm{SERS}}}{I_{\mathrm{bulk}}/N_{\mathrm{bulk}}}$$

where I_{SERS} and I_{bulk} denote the Raman scattering intensities from the 4-ATP adsorbed on the surface of NPGDF and the solid 4-ATP, respectively. N_{SERS} and N_{bulk} represent the numbers of the corresponding surface and solid molecules effectively excited by the laser beam, respectively. Based on the Raman

intensity of the a1 vibrational modes at 1576 cm^{-1} and b2 vibrational modes at 1435 cm^{-1} (Fig. S7, ESI†), the EF for a1 and b2 vibrational modes were calculated to be 3.1×10^4 and 5.5×10^5, respectively, also showing good SERS activity of the NPGDF substrate. Fig. 3F shows the optical image of NPGDF by OM platform of the Raman spectrometer. The profile of the dendritic α-Fe_2O_3 can be seen clearly, but the nanostructure and the Au NPs cannot be observed at all. Fig. 3F and G show area scanning mapping of the SERS spectra based on the intensity of the spectral band at 1140 cm^{-1} of 10^{-6} M 4-ATP. And it is interesting and important to find that the profile of Fig. 3G almost exactly coincides with Fig. 3F, which indicates the remarkable uniformity of the NPGDF as SERS substrate.

To further investigate the uniformity of this SERS substrate, a series of SERS spectra of 10^{-6} M 4-ATP (Fig. 4A) collected randomly from 50 spots and the relative standard deviations (RSD) of the intensities of the main vibrations were calculated, as shown in Fig. 4B–D corresponding to Fig. 4A, respectively. Above all, the main Raman vibrations of 4-ATP were obviously enhanced to a different extent at all spots of the NPGDF substrate within the boundary, while the values of the RSD for the vibrations at 1140, 1390 and 1435 cm^{-1} are 10.34, 11.72, and 13.09%, respectively, which are consistently less than 20%, further indicating the uniformity of the substrate.[30,31] It is also worth mentioning that the NPGDF was durable and stable under air ambient conditions for months. After storing at room temperature for three months, the NPGDF was employed to detect 4-ATP again and SERS signals could still be observed while the concentration of SERS probe was below 5×10^{-8} M (Fig. S8, ESI†).

Besides, the SERS activity of NPGDF was also evaluated by using CV as the probe molecule and well defined SERS spectra of CV verified further the high sensitivity of the NPGDF as substrate (Fig. S9, ESI†). Therefore, based on the above analysis, it is clear that the NPGDF exhibits high enhancement efficiency. This result can be explained with the fact that the nanoscale gaps between neighbouring Au NPs on the surface of NPGDF provide high density hot spots, and the close approach of two grafted Au NPs led to interaction of their localized surface plasmon resonances (LSPR). The LSPR of Au NPs is the result of the collective oscillation of conduction electrons within the particles upon interaction with light excitation, and this interaction was beneficial for SERS activity.[21,22] When excited by the incident radiation, a collective surface plasmon is trapped between the neighboring nanoscale gaps, thus creating a huge local electric field at these gaps. Also their rough surface possesses a high specific surface area which favors the adsorption of probing molecules and the formation of high density and uniform gaps is easy for NPGDF to capture probing molecules. Thus, it is not surprising that the NPGDF as SERS substrate performed with distinguished sensitivity and uniformity.

For a practical application, the NPGDF was also used as SERS substrate for pesticide analysis based on optical visualization strategy. As we know, pesticides are annually used to control pests of agriculture and forestry while they may cause problems of environmental pollution and also residues. Fig. 5A illustrates the principle of detecting pesticides with NPGDF as SERS substrate and series of SERS spectra of thiram at different concentrations. In this work, first, a droplet of solution containing NPGDF suspension and given concentration of pesticide molecules was added onto the solid target surface. And then, throughout the evaporation process under air ambient

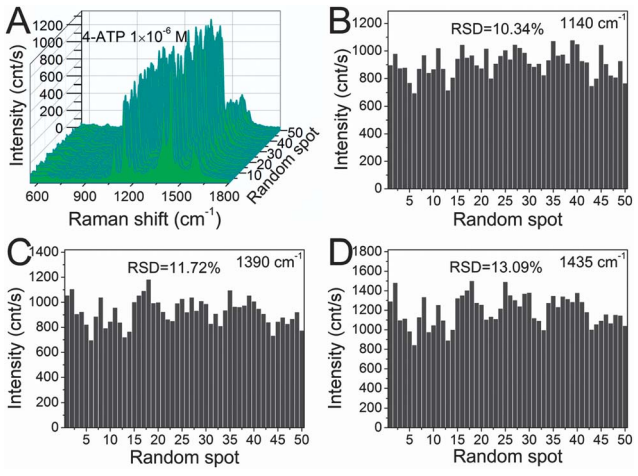

Fig. 4 (A) Series of SERS spectra of 10^{-6} M 4-ATP collected randomly from 50 spots of the NPGDF. (B), (C) and (D) are the intensities of the main vibrations of 10^{-6} M 4-ATP for the 1140, 1390 and 1435 cm^{-1} corresponding to (A) respectively.

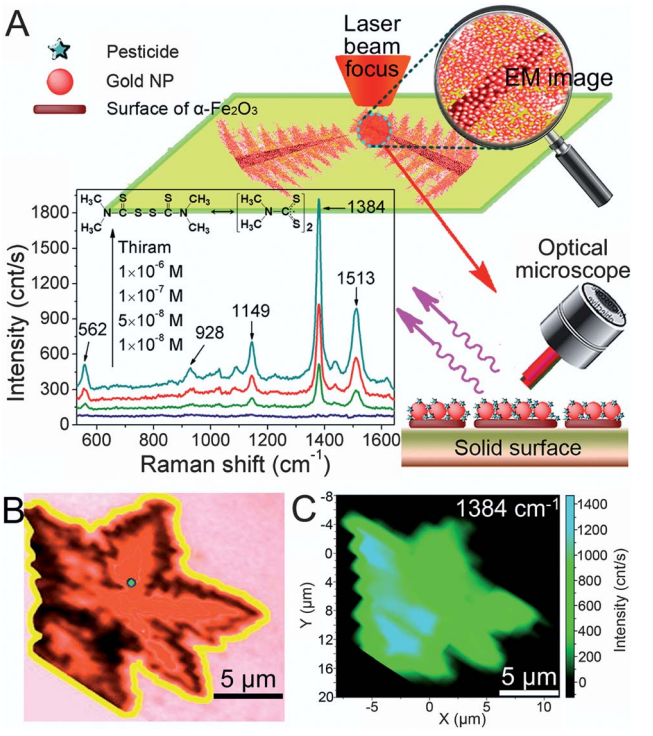

Fig. 5 (A) Schematic illustration of the principle to detect pesticide with NPGDF as SERS substrate and series of SERS spectra of thiram at different concentrations. (B and C) Optical image and the corresponding SERS spectral mapping based on the intensity of the spectral band at 1384 cm^{-1} of 10^{-6} M thiram.

conditions, pesticide molecules would interact with the Au NPs, resulting in pesticide molecules locating at the surface of the NPGDF, and the NPGDF microparticles will be adsorbed on the target surface, which can be seen clearly using the OM platform of a Raman spectrometer, thus ensuring the laser beam focuses on the efficient sites of the substrate within the boundary. The primary vibrations of thiram are confirmed according to the literature.[32] The SERS spectra area scanning mapping corresponding to the optical image (Fig. 5B) based on the intensity of the spectral band at 1384 cm^{-1} of 10^{-6} M thiram is shown in Fig. 5C, which also indicates the sensitivity and uniformity of the NPGDF as SERS substrate. The SERS of the 10^{-6} M thiram with NPGDF as the substrate and its RSD values for the vibrations at 1149, 1384 and 1513 cm^{-1} are 9.94, 13.64 and 12.33% (Fig. S10, ESI†), respectively, which are consistently less than 20%, also further demonstrating good uniformity and reproducibility of the substrate.

In addition, NPGDF can also be used for *in situ* detection of thiram residues on tea leaves, fruits and so on, just as shown in Fig. 6. Fig. 6A and B reveal the OM image with illustration of laser spot and Raman spectra on the blank surface of a tea leaf. The inset of Fig. 6A shows the OM platform of a Raman spectroscope and a sample of a tea leaf. In the absence of NPGDF, the Raman spectra could not be obtained for a fresh tea leaf due to the very strong fluorescence of the tea components.[33] Fig. 6C and D illustrate a typical OM image and Raman spectra of an uncontaminated tea leaf surface in the presence of NPGDF. As can be seen from Fig. 6C and D, by spreading NPGDF on the tea leaf surface, the profile of NPGDF can be observed by OM, while weak SERS spectra and fluorescence of clean surface were obtained. Fig. 6E and F show a typical OM image and Raman spectra on contaminated tea leaf surface with NPGDF as the SERS substrate. It is indicated that, after a fresh tea leaf has been contaminated with 5×10^{-6} M thiram and dried at room temperature in the fuming cupboard (*ca.* 1–2 h), a droplet of suspension containing NPGDF microparticles was added onto the surface. And then, throughout the evaporation process (*ca.* 1–2 h), thiram molecules would interact with the Au NPs, resulting in thiram molecules locating at the surface of the NPGDF, while the microparticles will be adsorbed on the tea leaf surface, which can be seen by the OM system. Thus, thiram residues can be detected. From Fig. 6E and F, it is indicated that strong SERS spectra of thiram on a contaminated tea leaf were obtained reproducibly. Besides, more tests on fruit (Fig. S11, ESI†) also confirmed the unusual ability of NPGDF in pesticide analysis.

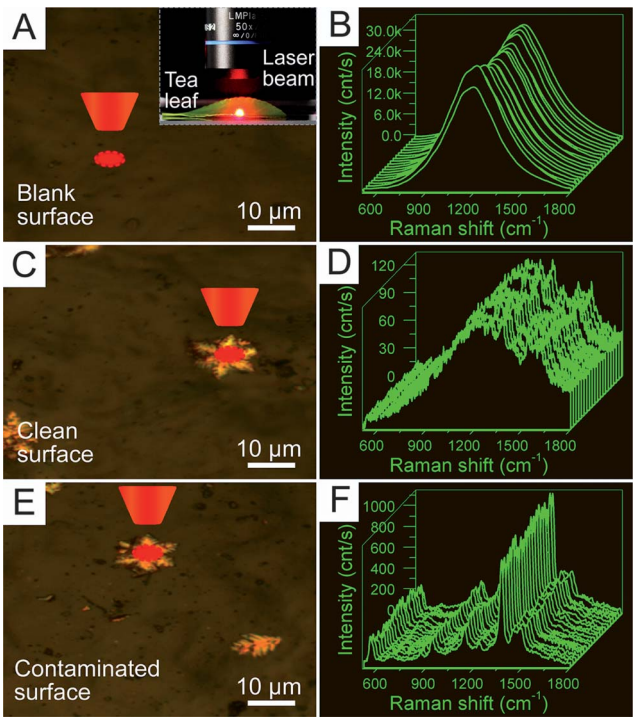

Fig. 6 *In situ* detection of thiram residues on tea leaves. (A and B) OM image with illustration of laser spot and Raman spectra on a blank surface of tea leaf. Inset of (A) is the OM platform of a Raman spectroscope and a sample of tea leaf. (C–F) are typical OM images and Raman spectra on uncontaminated and contaminated surface with thiram of tea leaf, respectively.

Conclusions

In summary, the designed and prepared Au NPs grafted on dendritic α-Fe_2O_3 as SERS substrate showed satisfying SERS sensitivity, uniformity and reproducibility by the optical visualization strategy. Using the OM platform of a Raman spectrometer, this substrate can be observed clearly, and the profile of the SERS spectral mapping with this substrate almost exactly coincides with the OM image, SEM image, TEM image and elemental mapping, which indicates the remarkable uniformity of the NPGDF as SERS substrate, thus ensuring the laser beam focuses on the efficient sites of the substrate under the OM platform. On the basis of this strategy, *in situ* and rapid detection of pesticide on tea leaves, fruits *etc*. can be achieved. Generally, the NPGDF as a highly sensitive and uniform SERS substrate with a feature of optical visualization exhibits great practical potentials for environment assessment and application of portable Raman spectrometers.

Acknowledgements

This work was supported by the National Basic Research Program of China (2011CB933700), the National Instrumentation program of China (2011YQ0301241001 and 2011YQ0301241101).

References

1 A. Samanta, K. K. Maiti, K. S. Soh, X. J. Liao, M. Vendrell, U. S. Dinish, S. W. Yun, R. Bhuvaneswari, H. Kim, S. Rautela, J. H. Chung, M. Olivo and Y. T. Chang, *Angew. Chem., Int. Ed.*, 2011, **50**, 6089–6092.
2 D. Cialla, A. Marz, R. Bohme, F. Theil, K. Weber, M. Schmitt and J. Popp, *Anal. Bioanal. Chem.*, 2012, **403**, 27–54.
3 R. A. Alvarez-Puebla and L. M. Liz-Marzan, *Chem. Soc. Rev.*, 2012, **41**, 43–51.
4 B. Sharma, R. R. Frontiera, A. I. Henry, E. Ringe and R. P. Van Duyne, *Mater. Today*, 2012, **15**, 16–25.

5 Y. Fang, N. H. Seong and D. D. Dlott, *Science*, 2008, **321**, 388–392.
6 M. J. Banholzer, J. E. Millstone, L. Qin and C. A. Mirkin, *Chem. Soc. Rev.*, 2008, **37**, 885–897.
7 K. Qian, H. Liu, L. Yang and J. Liu, *Nanoscale*, 2012, **4**, 6449–6454.
8 B. Yan, A. Thubagere, W. R. Premasiri, L. D. Ziegler, L. Dal Negro and B. M. Reinhard, *ACS Nano*, 2009, **3**, 1190–1202.
9 D. K. Lim, K. S. Jeon, J. H. Hwang, H. Kim, S. Kwon, Y. D. Suh and J. M. Nam, *Nat. Nanotechnol.*, 2011, **6**, 452–460.
10 Y. Zheng, T. Thai, P. Reineck, L. Qiu, Y. Guo and U. Bach, *Adv. Funct. Mater.*, 2013, **23**, 1519–1526.
11 S. Kim, J. H. Jin, Y. J. Kim, I. Y. Park, Y. Kim and S. W. Kim, *Nature*, 2008, **453**, 757–760.
12 T. Siegfried, Y. Ekinci, H. H. Solak, O. J. F. Martin and H. Sigg, *Appl. Phys. Lett.*, 2011, **99**, 263302.
13 L. B. Yang, H. L. Liu, J. Wang, F. Zhou, Z. Q. Tian and J. H. Liu, *Chem. Commun.*, 2011, **47**, 3583–3585.
14 L. B. Yang, L. A. Ma, G. Y. Chen, J. H. Liu and Z. Q. Tian, *Chem.–Eur. J.*, 2010, **16**, 12683–12693.
15 X. Li, G. Chen, L. Yang, Z. Jin and J. Liu, *Adv. Funct. Mater.*, 2010, **20**, 2815–2824.
16 J. A. Fan, Y. He, K. Bao, C. H. Wu, J. M. Bao, N. B. Schade, V. N. Manoharan, G. Shvets, P. Nordlander, D. R. Liu and F. Capasso, *Nano Lett.*, 2011, **11**, 4859–4864.
17 Z. Liu, B. L. Lv, D. Wu, Y. Zhu and Y. H. Sun, *CrystEngComm*, 2012, **14**, 4074–4080.
18 Y. Wan, J. Liu, W. Li, F. Meng, Z. Jin, X. Yu, X. Huang and J. Liu, *Nanotechnology*, 2011, **22**, 315501.
19 G. Frens, *Nature Phys. Sci.*, 1973, **241**, 20–22.
20 S. S. Dasary, A. K. Singh, D. Senapati, H. Yu and P. C. Ray, *J. Am. Chem. Soc.*, 2009, **131**, 13806–13812.
21 P. J. Schuck, D. P. Fromm, A. Sundaramurthy, G. S. Kino and W. E. Moerner, *Phys. Rev. Lett.*, 2005, **94**, 17402.
22 V. Liberman, C. Yilmaz, T. M. Bloomstein, S. Somu, Y. Echegoyen, A. Busnaina, S. G. Cann, K. E. Krohn, M. F. Marchant and M. Rothschild, *Adv. Mater.*, 2010, **22**, 4298–4302.
23 H. Liu, L. Yang, H. Ma, Z. Qi and J. Liu, *Chem. Commun.*, 2011, **47**, 9360–9362.
24 Y. Wang, H. Chen, S. Dong and E. Wang, *J. Chem. Phys.*, 2006, **124**, 74709.
25 S. Guo, S. J. Dong and E. Wang, *Small*, 2008, **4**, 1133–1138.
26 G. Hong, C. Li and L. Qi, *Adv. Funct. Mater.*, 2010, **20**, 3774–3783.
27 E. C. Le Ru, E. Blackie, M. Meyer and P. G. Etchegoin, *J. Phys. Chem. C*, 2007, **111**, 13794–13803.
28 X. M. Lin, Y. Cui, Y. H. Xu, B. Ren and Z. Q. Tian, *Anal. Bioanal. Chem.*, 2009, **394**, 1729–1745.
29 S. Tian, Q. Zhou, Z. Gu, X. Gu and J. Zheng, *Analyst*, 2013, **138**, 2604–2612.
30 R. H. Que, M. W. Shao, S. J. Zhuo, C. Y. Wen, S. D. Wang and S. T. Lee, *Adv. Funct. Mater.*, 2011, **21**, 3337–3343.
31 Q. Shao, R. H. Que, M. W. Shao, L. Cheng and S. T. Lee, *Adv. Funct. Mater.*, 2012, **22**, 2067–2070.
32 B. Liu, G. Han, Z. Zhang, R. Liu, C. Jiang, S. Wang and M. Y. Han, *Anal. Chem.*, 2012, **84**, 255–261.
33 L. Zeiri, *J. Raman Spectrosc.*, 2007, **38**, 950–955.